PHYSICAL REVIEW C VOLUME 8, NUMBER 3 SEPTEMBER 1973

Elastic Muon-Carbon Scattering in a Low-Momentum-Transfer Region*

T. Sanford,† S. Childress, G. Dugan, L. M. Lederman, and L. E. Price
Columbia University, New York, New York 10027

(Received 23 February 1973)

Elastic scattering of 190-MeV/c muons has been measured to ~1% in the angular range 140 mrad$\leq\theta\leq$590 mrad corresponding to invariant four-momentum transfers 0.016 fm^{-2} $\leq q^2 \leq$ 0.33 fm^{-2}. Magnetostrictive wire spark chambers were used to measure the incident momentum and scattering angle. A comparison is made with electron scattering experiments which extend down in q^2 to 0.02 fm^{-2}. A change of slope of the carbon form factor in the range below 0.05 fm^{-2} would indicate unexpected structure in the outer regions of the nuclear charge distribution. Disagreement with electron scattering where both processes are measured would indicate a breakdown of muon-electron universality. No such effects are observed.

I. INTRODUCTION

Although nuclear and nucleon charge distributions have been studied extensively, there is relatively less information on the behavior of the outer regions of the charge distribution as would be observed in small angle lepton scattering.

Recently,[1,2] there has been speculation that the proton may have a small amount of its charge extending to a large distance from its central core—in short, the proton may have a "halo." This speculation has raised the question of how the halo would look in a nucleus and the further question: Do nuclei have halos resulting from the individual proton wave functions having a small probability of extending to a large distance from the nuclear core?

The work reported here was to answer this second question for the specific case of the carbon nucleus by measuring the elastic muon-carbon cross sections at the Nevis cyclotron. The high muon-carbon sections and small radiative corrections make this approach competitive with that of electron scattering.

Previous elastic electron-carbon and muon-carbon experiments[3-13] have measured the cross section over the q^2 region of 0.02 to 16 fm^{-2}. Scattering in the region of moderate momentum-transfer ($q^2 > 1$ fm^{-2}) probes the nuclear core, but is rather insensitive to the nuclear surface. Most of the previous experiments[3-12] accordingly establish the rms radius of the distribution of charge in the core. For low-momentum-transfer scattering ($q^2 < 0.5$ fm^{-2}), the incident projectile is scattered by the outer regions as well as the inner regions of the nucleus and accordingly is sensitive to the entire distribution of charge. A scattering experiment in this q^2 domain then determines the rms radius of the entire charge distribution.

Measurement of the $2P$ to $1S$ x-ray energy transition in muonic carbon also provides a measure of the rms radius at low q^2. However, the energy shift in the transition due to the finite size of the nucleus is proportional to Z^3, so that, for light nuclei such as carbon, the precision of the measurement is low and only large limits can be placed on a halo.[14] Jansen, Peerdeman, and de Vries[13] have performed the only precise elastic electron-carbon scattering experiment in the low q^2 region. A comparison of the radii obtained from their data with those obtained here provides somewhat different information on the relation between the muon and electron and is a useful byproduct of the investigation reported here.

II. EXPERIMENT

The experiment was designed to measure the incident muon momentum and angle into a carbon target and the resulting outgoing angle. In addition, because there were also charged pions, electrons, and neutral particles in the beam, the design allowed muons to be distinguished from these unwanted particles. The following summarizes the three major considerations that enabled the total cross section over the q^2 range 0.016 to 0.33 fm^{-2} to be determined to ~1% or the rms radius to be determined equivalently to ~6%.

(1) The primary problem arose from the large flux of pions present in the muon beam and the large pion-to-muon cross-section ratio over the above q^2 range. The beam had typically a 6/1 pion-to-muon ratio and at $q^2 \simeq 0.01$, and $q^2 \simeq 0.3$ fm^{-2} the cross section ratios are 10/1 and 100/1, respectively.[15] To keep the absolute error in the determination of the radius below 6% it was therefore necessary to reduce the fraction of pions in the beam by at least 2000. This reduction was achieved by measuring the time of flight (TOF) of the particles between pairs of counters placed before the target and selecting only those particles that correspond to a muon TOF. Multiply redundant determination of the particle's TOF

between other pairs of counters and range information after scattering were used to check that this suppression factor was attained.

(2) A second problem resulted from the large multiple Coulomb scattering (MCS) at small momentum transfers. For a 0.6-cm-thick carbon target and a 100-MeV/c incident muon beam the MCS in the target increased the probability of observing a scattered event in a small bin centered about $q^2 \sim 0.01$ fm^{-2} by 20%. Because the MCS was inversely proportional to momentum, a high momentum beam was advantageous. Muon beams from the Nevis cyclotron were limited to momenta below 220 MeV/c and a reasonable compromise between achieving flux and limiting MCS was made by choosing an average beam momentum of 195 MeV/c.

(3) A third problem resulted from the $1/P^2\theta^4$ behavior of the cross section. In order for the absolute uncertainty in the cross section to be kept below 1%, the absolute momentum needed to be measured to better than 0.5% and the scattering angle to better than 0.3%. This requirement was achieved by using magnetostrictive (MS) spark chambers coupled with a dipole magnet to measure the incident momentum and scattering angle.

Figure 1 shows the experimental arrangement. The outside dipole separated the charged-particle beam from the neutral one. TOF measurements between scintillation counters C_1, C_2, C_3, and H and penetration through the 2.8-cm-thick Pb wall, hodoscope, and range counters distinguished muons from pions and electrons. The spectrometer, which consisted of a dipole and of six MS wire spark chambers, measured the incident muon's momentum and angle into a carbon target, and the three spark chambers after the target measured the muon outgoing angle. A scatter greater than 100 mrad was indicated by counter S in anticoincidence with counters C_1, C_2, C_3, and H. Data were stored on line to the Nevis 360/44 computer. The following gives details on the counter system, chamber system, and data recorded.

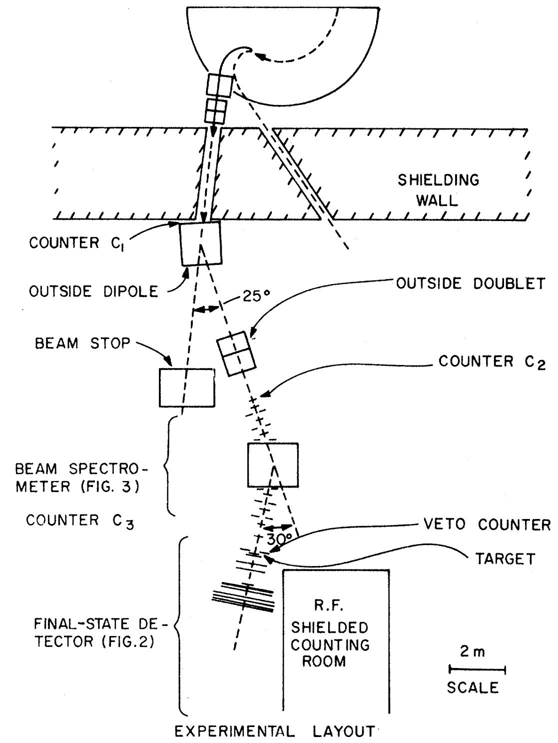

FIG. 1. Plan view of experiment showing cyclotron, transport magnets, and neutral beam stop.

A. Counter System

1. *Size and Location of Counters*

The beam incident to the spectrometer was defined by 0.6-cm-thick plastic scintillation counters C_1 and C_2, which had 20×20-cm^2 and 13×13-cm^2 areas, respectively. In order that the transit time between counters C_1 and C_2 could be measured precisely, each counter had Amperex XP 1021 phototubes on two opposite sides. The outputs of both phototubes went to a time averager circuit, which produced a timing signal corrected for the position of the particle within the counter. To minimize MCS in the spectrometer and target regions, only one thin counter C_3 (1 mm thick with a 13-cm diam) was placed between C_2 and the target. Over this region, the beam was collimated by a

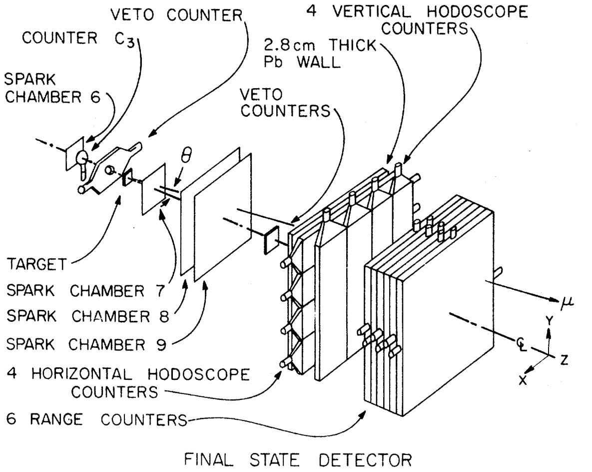

FIG. 2. Apparatus for detecting scattered muon. Particle must miss counter S and go through the lead wall and hodoscope to be accepted. Range is measured in liquid scintillation counters.

series of large veto counters $V_1, \ldots, V_{20}$ that had approximately 15×15-cm^2-square apertures. The rms angular divergence of the beam at the target was ±12 mrad and the rms momentum spread was ±3.6%. The charged beam defined by the counter coincidence $C_1 \cdot C_2$ had a typical rate of 10^5/sec.

The 33×33-cm^2-square S counter was located about 125 cm downstream of the target, so that scatters in the target greater than 100 mrad could drift out of the beam and miss S (Fig. 2). The hodoscope array H and range counters $R_1, \ldots, R_6$ located on the downstream side of the Pb wall then detected and measured the range of those particles that scattered through less than 700 mrad. The Pb wall absorbed 20% of the pions but allowed muons for all scattering angles to pass freely and, on the average, stop in R_4. The hodoscope array consisted of two planes of counters $H_{\text{horizontal}}$ and H_{vertical}. Each plane was made of four $1.3\times 46\times 183$-cm^3 counters. Each H_h counter had two RCA 8575 phototubes one mounted at either end of the counter, with their time averaged signal being used for a TOF measurement between C_1 and H_h. The H_v counters had just one RCA 8575 phototube connected at an end. To minimize the effect of a 1 to 2% particle-detection inefficiency per counter, all hodoscope signals were summed to form a signal "H." Each range counter was a $2.5\times 214\times 214$-cm^3 vat of liquid scintillator with 0.32-cm-thick Plexiglas walls that had four RCA 8575 phototubes mounted on three of its 2.5×214-cm^2 edges. The outputs of the four tubes were connected together and formed a single signal for each counter.

2. *Scattered Event Trigger*

The logic signal

$$F_\mu = \langle C_1\rangle \cdot \langle C_2\rangle \cdot C_3 \cdot H \cdot \left(\sum_{i=1}^{20} \overline{V}_i\right)$$

measured the incident muon flux, and the anticoincidence of S and F_μ defined the scattered event trigger. The brackets $\langle\ \rangle$ indicate a time-averaged signal. The time delay and width of the coincidence between counters C_1 and C_3 were used to regulate the percentage of pions and electrons in F_μ. Typically, they were set such that the ratios of π/μ and e/μ were less than 1% in the scatter trigger. Owing to the beam dispersion and the tight time coincidence between C_1 and C_3 the typical F_μ ratio was only ~500/sec, and the scattering rate was ~1/sec.

B. Chamber System

1. *Parameters and Resolutions*

The six momentum-measuring spark chambers 1–6 were grouped into two sets: chambers 1–3 and chambers 4–6. The six chambers each had an active area of 15×15-cm^3 and a 0.6-cm gap, and the three chambers within a set were spaced by 51 cm. The two sets were held fixed to one another by long aluminum channels, which formed a 30° angle inside the dipole.

To minimize the effect of MCS in the chamber system, the chamber windows were constructed of 13-μm Mylar and He bags with 13-μm Mylar windows were spaced between all chambers. The chambers were wound with 100-μm diam aluminum wire spaced every millimeter. The time corresponding to a spark position was scaled by a 20-MHz clock. This time resolution corresponded to $\frac{1}{4}$ mm in space, and the chamber resolution was 0.38 mm. The resolution of the angle as determined by straight-line fits to the sparks in chambers 1–3 or 4–6 was 0.7 mrad.

The three scattering-angle measuring chambers 7–9 were separated by about 25 cm and had active areas increasing from 41×41 cm^2 to 92×102 cm^2, which allowed scattering angles up to 700 mrad to be measured.[16] The windows were made of 25-μm Mylar, and no He bags were placed between the chambers. Accordingly, the resolution of the angle, as determined by straight-line fits to sparks within the chambers of this set, was slightly larger than that of the momentum measuring sets (1 mrad).

The over-all momentum and scattering-angle resolution was 0.6% and 10 mrad, respectively.

2. *Position and Angle Calibration*

The spark chambers were calibrated by associating the measured delay times with known particles positions in the chambers. In this manner the time vs X or Y position slope was determined to 0.1% for the small momentum measuring chambers and 0.2% for the larger scattering-angle chambers. Straight-line fits to the spark positions in chambers 1–3, 4–6, and 7–9 determined the necessary angles. The absolute uncertainty in the angle defined by chambers 1–3 and 4–6 and by the scattering angle was 0.14, 0.14, and 0.28% of the angle, respectively.

The possibility existed that the effective X or Y position of the spark position within a chamber might change with angle of traversal through the chamber owing to the dynamics of spark breakdown. A reasonable model predicts that the change in lateral position should be proportional to the angle of traversal.[17] Such a shift with angle can be approximately accounted for by assuming a different distance between chambers than was measured.

In order that this effective distance could be evaluated, a series of special runs was made at the conclusion of the experiment. The entire assembly of scattering-angle chambers was rotated about an axis normal to the floor through known x angles, θ_R. For each θ_R, all spark chambers were triggered on F_μ. By measuring the difference between two measured x positions in scattering-angle chambers i and j, the incident angle defined by chambers 4–6, and θ_R, the effective distance between chambers i and j was determined. The difference between the effective distance for chambers 7, 8 or 7, 9 was about 1%, or 0.25 cm.

3. *Momentum Determination*

The momentum of the incident particle, P, was determined by measuring its bending angle in traversing the 18H36 spectrometer dipole (Fig. 3). A precise determination of P depended on (1) knowing θ_B, the angle that the 1-3 spark chamber set made with the 4–6 set and (2) knowing the integral of the magnetic field along the particle trajectory. θ_B was measured to 0.03 and 0.07% by two independent techniques. The results of both measurements agreed with each other to 0.08%. Before the experiment, the dipole was shimmed to give a high uniformity in $\int B_y dz$ so that corrections to the momentum measured by assuming a circular trajectory within the effective field of the dipole were less than 0.7%. The field was measured in one quadrant of the dipole's median plane ($x > 0$, $y = 0$, $z > 0$) and the entire field was obtained by fitting a multipolar expansion of $B_y(x, 0, z)$ to the measured values.[18] In the central region of the dipole the field was measured to 0.01% using a nuclear-magnetic-resonance (NMR) probe, and in the fringing field region the field was measured to 1% using a Hall probe. The symmetry of the field was tested by measuring the field at symmetrical values of x and z. These measurements indicated that any corrections in the $\int B_y dz$ due to asymmetries in $\overline{B}$ in the x or z directions were less than 0.025%. The $\int B_y(x, 0, z)dz$ was checked by using a flip coil. The results of the flip-coil measurements agreed with a numerical integration of the fitted value of $B_y(x, 0, z)$ to better than 0.1%.

Recorded with each event was the central field of the dipole as measured by a NMR probe. This measurement, together with the knowledge of θ_B and the 1–6 chamber positions, enabled P to be determined. The absolute uncertainty in the determination of P was 0.14% which was the result of the following uncertainties taken in quadrature: (1) 0.08% uncertainty in θ_B; (2) 0.1% uncertainty in $\int B_y dz$; (3) 0.02% uncertainty resulting from a 0.1% uncertainty in chamber 1–6 calibrations; and (4) 0.04% uncertainty resulting from approximations used in deriving P.

4. *Check of Momentum-Scattering-Angle Calibrations*

During the experiment the angular distribution of 7.5×10^4 pion decay events was measured. For these runs, H was left out of the scatter trigger, and the time coincidence between counters C_1 and C_3 was adjusted for pions. These events were

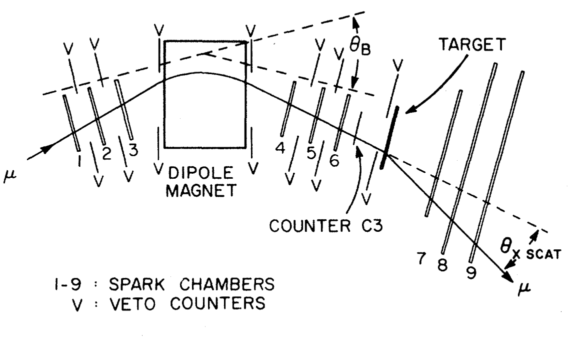

SPARK CHAMBER SYSTEM (NOT TO SCALE)

FIG. 3. Arrangement of spark chambers to measure incoming momentum and scattering angle.

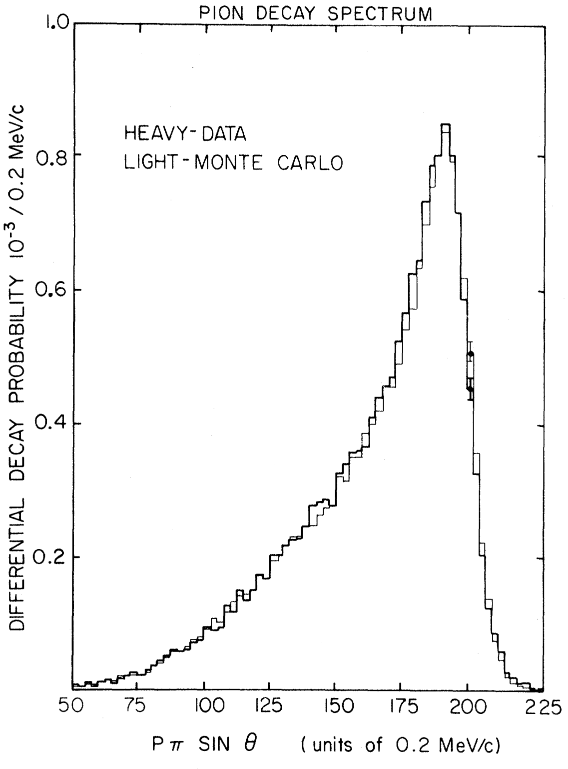

FIG. 4. Observed pion decay spectrum compared with Monte Carlo prediction as a check of calibration of momentum and angle.

used to check the scattering angle and momentum calibration. The pion decay process was simulated by generating Monte Carlo events in the computer. The resulting Monte Carlo spectrum in the variable $Q = P_\pi \sin\theta$ was fitted to the measured Q spectrum (Fig. 4) by varying the scale of Q. The optimum fit gave a χ^2 of 100 for 96 degrees of freedom $(ND)^7$ and showed that the scale of Q should be expanded by $(0.24 \pm 0.1)\%$. This fit was consistent with the 0.14% calibration error in P and the 0.28% calibration error in θ.

C. Data

1. *Data Acquisition System*

The data acquisition system consisted primarily of a Science Accessories Corporation (SAC) control unit and a scaler unit that encoded the spark positions. The units that recorded counter bits, TOF's, and the field of the spectrometer dipole were all interfaced to the SAC control unit. The counters were scaled by a bank of 40 Societe d'Electronique Nucleaire scalers (SEN system) and the combined SAC and SEN systems were interfaced to the Nevis IBM 360/44 computer.

2. *Data Recorded with Each Event*

The apparatus was triggered by a muon scatter. In addition, the apparatus was triggered randomly on F_μ, in order that momenta, TOF spectra, and spark chamber inefficiencies could be monitored for the beam, free of any scattering-angle bias (Fig. 5). With each trigger, spark chambers were fired, dead times set, and gates opened, allowing the following information to be transmitted directly to the computer: (1) two X, Y spark coordinates per chamber; (2) bits indicating which hodoscope and range counters were on; (3) TOF's between counters C_1, C_2, C_3, and H; and (4) the central magnetic field of the spectrometer dipole as measured by a NMR probe. The incident muon flux and other counter coincidences scaled were periodically transmitted and stored in the computer.

3. *Data Accumulated*

2.4×10^5 muon scattering events were accumulated using two $15 \times 15\text{-cm}^3$ carbon targets of thickness 0.6 and 0.3 cm. The two thicknesses allowed the effects of MCS to be studied. In order that a high geometrical efficiency for detecting small and large angle scatters could be achieved, the target was placed in two different positions along the beam line: (1) in an "upstream" position close to counter C_3 and (2) in a "downstream" position close to spark chamber 7. In addition, so that background scattering events coming from muon scatters in the air and counters could be subtracted from the data, the target was periodically removed and events were accumulated with no target present.

III. EVENT SELECTION

The data were reconstructed and summed with the aid of a computer-analysis program. Before the reconstructed data were summed, each event was required to satisfy selection criteria (cuts) which ensured that the encoded events were muon-scattering events and were unambiguously reconstructed. For each cut, the incident flux was suitable corrected.

The flux correction was obtained by observing the fraction of randomly selected beam events that were lost by the given selection criteria. The flux correction found in this manner was independent of scattering angle for cuts applied to the particle before it scattered in the target—both beam muons that did and did not scatter had a similar angular and spatial structure upstream of the target and therefore traversed similar regions of the counters and spark chambers. However, the same was not true for cuts applied to the particle after it had passed through the target, so care was taken to ensure that no angular bias was introduced at a level greater than ~0.1%.

Four types of cuts were applied to the data. The four types with the percentage of accumulated flux remaining after successively applied cuts were:
A. cuts ensuring that the scattered particle was a muon, 56%;
B. cuts ensuring a reconstructable incident momentum and incident angle into the target, 36%;
C. cuts ensuring a reconstructable scattering

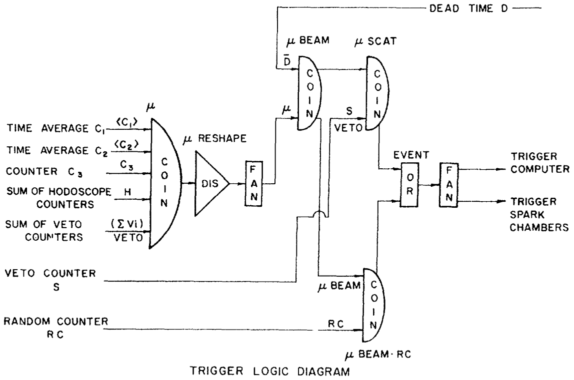

TRIGGER LOGIC DIAGRAM

FIG. 5. Trigger logic for experiment. In addition to muon scatters, a random sample of unscattered muons is accepted in order to measure the properties of the incident beam.

angle, 35.9%;
D. cuts eliminating background, 35.9%.

A. Cuts Ensuring that the Scattered Particle Was a Muon

Pions and electrons were suppressed in the trigger by the tight time coincidence between counters C_1 and C_3. The parameters of the coincidence were varied, changing the percentage of pions and electrons in the beam and thereby allowed the effects of these particles to be studied. The recorded range and TOF's between C_1C_2, C_1C_3, C_1H, and C_3H enabled the percentage of the contaminants to be estimated and the shapes of the respective C_1C_2 and C_1C_3 β spectra to be evaluated (Figs. 6 and 7).

Typically, the C_1C_3 coincidence was set corresponding to $0.86 \lesssim \beta_{C_1C_3} \lesssim 0.92$ and under these conditions the percentage of pion and electrons in the trigger was ~1%. About 80% of the pions in the trigger resulted from pion decay rather than from pion scattering, so that after a target-out background subtraction was made, the real pion contamination was only ~0.2%. To ensure a pion and electron contamination of less than ~0.01 and ~0.5%, $\beta_{C_1C_2}$ and $\beta_{C_1C_3}$ were required to lie within (0.86, 0.915).

B. Cuts Ensuring a Reconstructable Momentum

The position of the particle in two out of three chambers located on either side of the spectrometer dipole was sufficient to allow the incident momentum and the incident angle into the target to be determined. This knowledge of positions in two out of three chambers was a first criterion. The individual momentum chamber inefficiency for single tracks was 2%, so this cut lost only 0.04% of the events.

A serious loss of events resulted however from the high incident flux, which ran between 30 to 100×10^3/sec in the first set of chambers. Owing to the long sensitive time (~1 μsec), the chambers frequently broke down along old trajectories as well as along the one that produced the trigger. These multitrack events resulted in an ambiguity as to which track was associated with the trigger. In order that these ambiguities would be removed, it was required that at least two spark chambers on either side of the dipole have exactly one spark within a chamber boundary.

The above criteria give a trajectory, but they did not ensure that the correct trajectory had been obtained. Two further restrictions were therefore imposed. First, when three sparks were observed in one of the sets of three chambers, the three sparks were required to fall on a straight line, within the MCS and spark-chamber jitter (~0.5 mm). Second, the entire trajectory on either side of the dipole was required to be consistent with the resulting momentum determined from the angle measured in chambers 1–3 and 4-6.

C. Cuts Ensuring a Reconstructable Scattering Angle

In order for the scattering angle to be determined, the position of the particle in only two of the three angle measuring chambers was required (assuming the above set of cuts). Again, this knowledge was the first criterion. The individual angle chamber inefficiency for single tracks was ~2% and fluctuated by ~1% over the active area of the chamber. The efficiency as a function of angle showed no change within ~1% as the angle was increased to 30°.

About 90% of the scattered events gave both a single track in chambers 7–9 and a reasonable scattering point when projected back to the target. The remaining 10% of the events were mainly two-

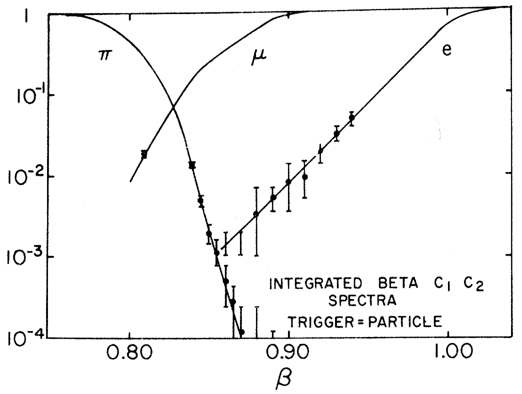

FIG. 6. Integrated incident β spectrum as measured by time of flight between counters C_1 and C_2.

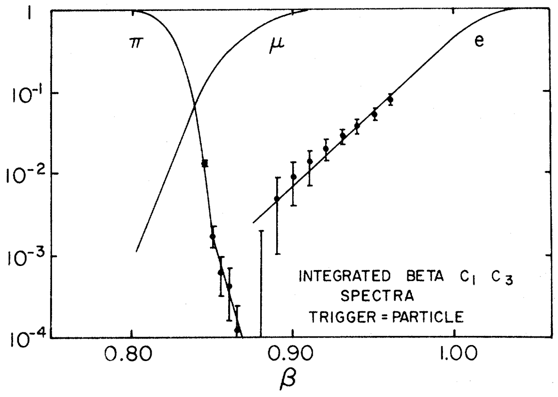

FIG. 7. Integrated incident β spectrum as measured by time of flight between counters C_1 and C_3.

track ones in which one, two, or three sparks were missing. To ensure that the elimination of the multispark events would not bias the angular distribution, these events were included in the analysis.

The multispark events were unscrambled by using the requirement that the track formed by some combination of sparks in chambers 7–9, when projected to the target, agree with the X and Y positions obtained when the track formed by sparks in chambers 4–6 was projected to the target. The remaining ambiguities were usually eliminated by projecting the tracks to the hodoscope plane and observing which track intersected the "on" hodoscope counter. Failing this, the track that projected closest to the correct scattering point in the target based on the chambers 4–6 projection or that gave the best fit to a straight line was ultimately chosen. If the fit was poor, the wrong combination of sparks was assumed to have been selected. The optimum two-spark trajectory was then taken as representing the correct track.

With the inclusion of the multispark events, for all carbon scattering events, where the particle passed through the scattering-angle chambers, ~99.7% of the events gave a trajectory that predicted a scattering point within ±2.5 cm of that predicted by projecting chambers 4–6 to the target

TABLE I. Magnitude of corrections for the 0.6-cm carbon data.

		θ(mrad)		
		100 (%)	250 (%)	600 (%)
(a)	Background scattering	6	6	6
(b)	Geometrical inefficiency	60	0	30
(c)	Chamber resolution and MCS	16	1.5	0.6
(d)	Momentum spread and loss	3	4	5
(e)	Inelastic scattering	0.3	1.4	10

D. Cuts Eliminating Background

65% of the background resulted from the muon scattering in the air, counters, and chambers; and 35% resulted from the muon decaying. This background manifested itself by producing a scattering point not in the target. For the 0.6-cm carbon data, 23% of the observed scattering events were background. This background was reduced to 6% by requiring (1) that the projection of chambers 7–9 to S be outside a $23\times23\text{-cm}^2$ square centered on the $33\times33\text{-cm}^2$ S counter, and (2) that the projection of tracks in 4–6 and 7–9 meet within a $2.5\times2.5\times13\text{-cm}^3$ volume at the target, the long length corresponding to the beam direction. These requirements were checked using the experimental rotation runs and the Monte Carlo program to ensure that at a level of ~0.1% the cuts

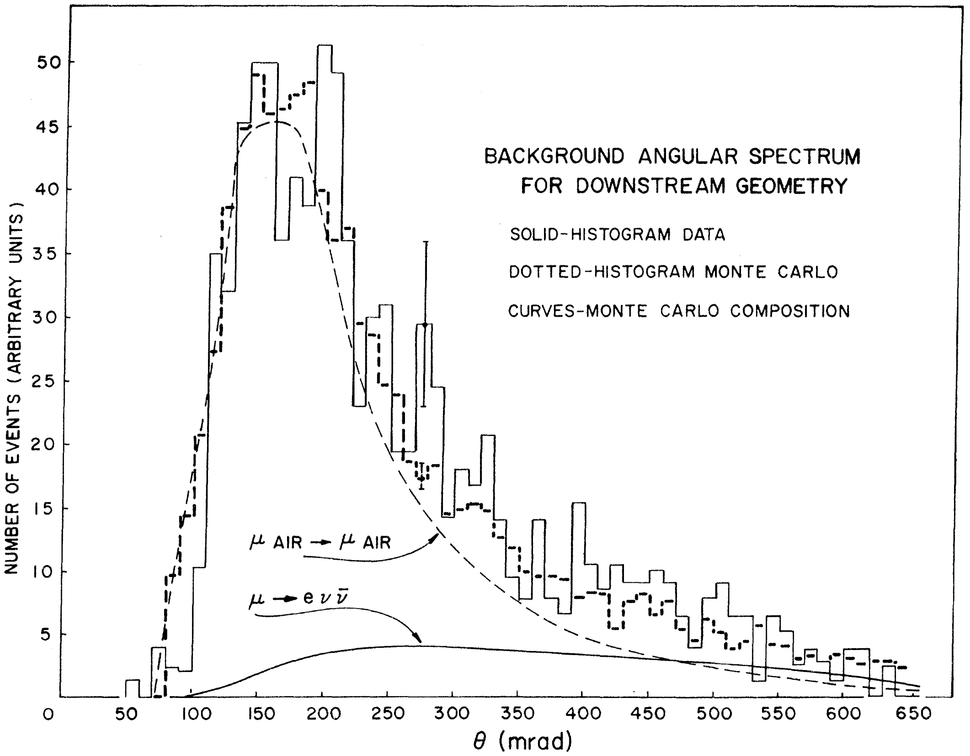

FIG. 8. Target-out background for target downstream: data and Monte Carlo prediction.

did not affect the angular distribution of muon scattering events coming from the target.

IV. SUMMED-EVENT CORRECTION

The reconstructed data that satisfied the above selection criteria were summed to obtain an experimental cross section as a function of θ. Before this cross section was compared with the electron-carbon cross sections, the effect that the measuring apparatus had on the observation was removed. Impurities in the carbon target, random veto in S concurrent with a valid scatter, muons stopping in the Pb wall, inefficiency of hodoscope counters, accidental triggers, flux scaler malfunction, and data-transfer malfunction all introduced corrections of less than 0.1% with the exception of the ramdom veto of S which introduced a 0.25% correction for a fraction of the runs. However, important corrections arose from: (a) acceptance of events that did not come from muon scattering in the carbon target (i.e., background events); (b) geometrical inefficiency at small and large scattering angles; (c) chamber resolution and the MCS in the target, air, counters, and chambers; (d) acceptance of a broad band of incident momenta and the momentum lost by the muon in traveling the distance between the spectrometer, where the momentum was measured, to the target; and (e) acceptance of inelastic scattering events. The magnitude of these corrections for the 0.6-cm carbon data is tabulated for the angular end points and a midpoint in Table I.

The necessary corrections were found using the theoretical first-order Born cross section for elastic muon-carbon scattering based on the shell-model form factor that best fit the low q^2 electron-carbon data. Specifically, Bentz's parameters[11] were used, and the corrections to the data were obtained from the ratios of the theoretical number of events, modified by the apparatus in a small angular bin centered about θ, divided by the theoretical number of events in the θ bin.

The dependence of the ratio on the form factor was checked for form-factor variations that spanned the range of a constant form factor to the Bentz form factor. The variations in the calculated ratios were always less than a few tenths of a percent.

A number of corrections relied on a Monte Carlo simulation of the apparatus. The program simulated the propagation of either muons or pions from spark chamber 4 to the downstream edge of the Pb wall. The initial positions X, Y, angles X', Y', and momentum P beam distributions were obtained by randomly sampling from the actually measured X, Y, X', Y', and P beam distributions. The sampling was done using two-dimensional plots of these variables in order that the position

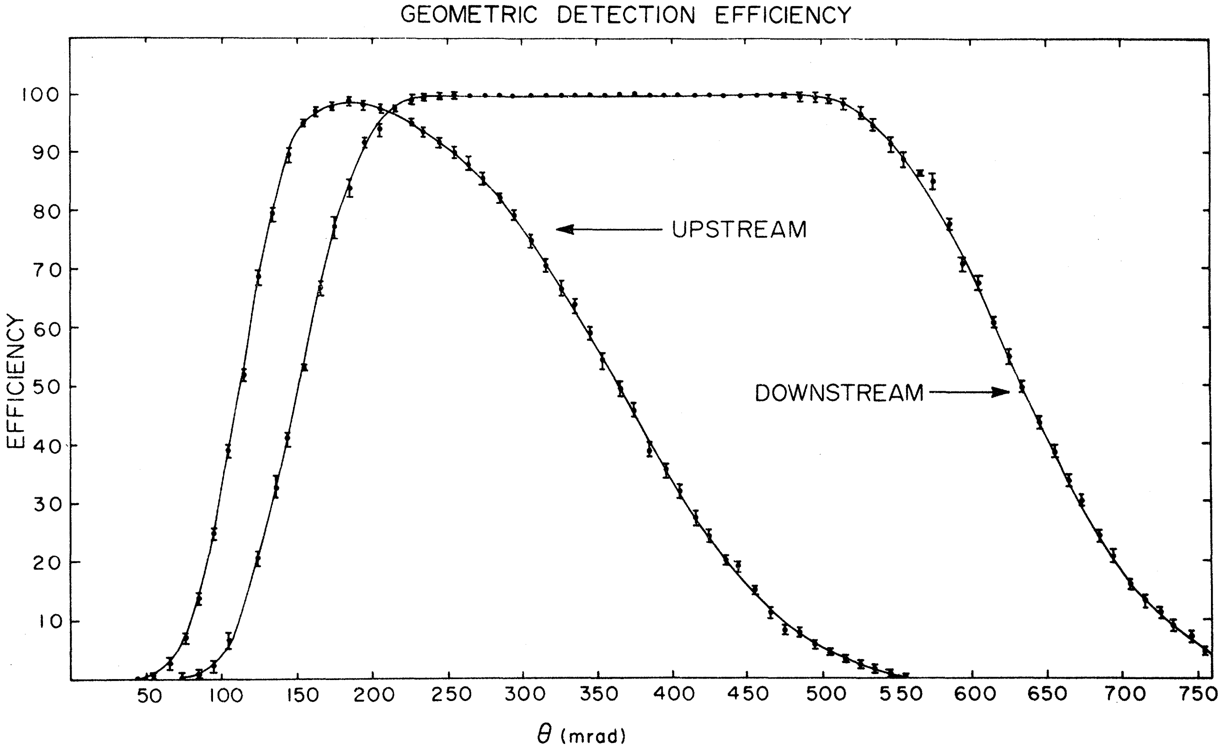
GEOMETRIC DETECTION EFFICIENCY

FIG. 9. Geometric efficiency as a function of scattering angle for the two target positions.

and the angle correlations with momentum were reproduced. Each event was then propagated through the various regions of the system, and in each region the particle was allowed to both decay and MCS as well as single scatter, according to the Goudsmit-Saunderson (GS)[19] and Fermi[20] distributions; energy loss, which was only a few MeV over the entire chamber system, was neglected, except for the pion decay simulation.

A. Background Subtraction

While the experiment was being run, the carbon target was periodically removed, and data were accumulated without the target. Owing to MCS in the target, the target-out events could not be subtracted directly from the target-in events to produce a distribution of muon-carbon scattering free of background.

The effect of the target on the background events that produced a trigger was studied by using the Monte Carlo program to generate events for no target in place (Fig. 8), and then using the same random-number sequence repeating the event generation with a carbon target in place. The results of the Monte Carlo program were then used to correct the target-out data for lack of MCS in the target before the target-out data were subtracted from the target-in data. Although the correction to the target-out data was as large as 40% for small angles, the total background was only 6% for 0.6-cm C target, and at angles above 140 mrad, the correction changed the over-all normalization by only 1 to 2%.

B. Geometrical Acceptance

The number of Monte Carlo events in a measured scattering-angle bin that succesfully passed through all the scattering-angle chamber apparatus, hodoscope counters, and avoided hitting S, compared to the total number of events that started out in that angular bin measured the efficiency directly (Fig. 9). The dependence of the efficiency function on the input distribution was examined by comparing the results for two input distributions as measured at different points along the beam line. By using the projected X and Y beam distribution at the target along with X' and Y' determined from chambers 4–6, all correlated with P, as input distributions to the Monte Carlo, rather than those distributions measured at X_4. The resulting efficiency functions agreed with the one calculated using the distributions within the 0.5% statistics per 10-mrad bins.

Table II indicated the systematic error in the efficiency function. This error arose primarily from the uncertainty in the position of the S counter along the beam line and from the uncertainty in the spark position for large scattering angles at the scattering-angle chamber boundaries. For the upstream data, the position of S was measured to ±0.6 cm, and for the downstream data, the position was measured to only ±1.2 cm. For large scattering angles, the lateral position of the spark in a chamber had a jitter of ~0.25 cm and at these angles the average deviation between the actual particle position and where the spark formed was uncertain also to ~0.25 cm.

C. Chamber Resolution and MCS

The effect of MCS in the target, in the air, and in the chambers and the effect of chamber resolution were calculated analytically using the GS distribution. The calculation of these corrections was checked over the region 150–400 mrad using the Monte Carlo program to simulate the MCS and chamber resolution. Over this region the Monte Carlo results agreed with the analytical calculation to better than 0.1%.

D. Incident Momentum Spread and Momentum Loss

The effect of the 3.6% incident momentum spread on the efficiency corrected angular spactrum was evaluated using the measured random-beam momentum distribution. Account was taken of the small momentum loss (typically 2 MeV/c) in propagation of the muon from the spectrometer, where the momentum was measured, to the target, where the muon scattered. The total correction to the cross section was 3.5%.

TABLE II. Comparison of geometrical effeciencies calculated using two different cross sections at the carbon target.

	Upstream geometry		Downstream geometry	
θ (mrad)	Efficiency (%)	Systematic error (%)	Efficiency (%)	Systematic error (%)
55	0.6 ± 0.03	±0.1		
105	38.8 ± 0.7	±0.6	6.7 ± 1.5	±0.65
155	95.1 ± 0.5	±0.3	53.6 ± 0.4	±2.7
205	97.5 ± 0.2	±0.6	94.4 ± 1.0	±0.5
255	89.7 ± 0.9	±1.0	100.0 ± 0.0	±0.0
305	74.9 ± 1.1	±1.5	100.0 ± 0.0	±0.0
355	54.6 ± 1.3	±2.4	100.0 ± 0.0	±0.0
405	31.5 ± 1.3	±1.4	100.0 ± 0.0	±0.0
455	15.0 ± 0.5	±0.6	100.0 ± 0.0	±0.0
505	3.7 ± 0.3	±0.2	99.2 ± 0.3	±0.4
555			89.1 ± 0.3	±0.5
605			67.8 ± 0.7	±2.4
655			39.2 ± 0.8	±1.4
705			15.9 ± 1.0	±0.6

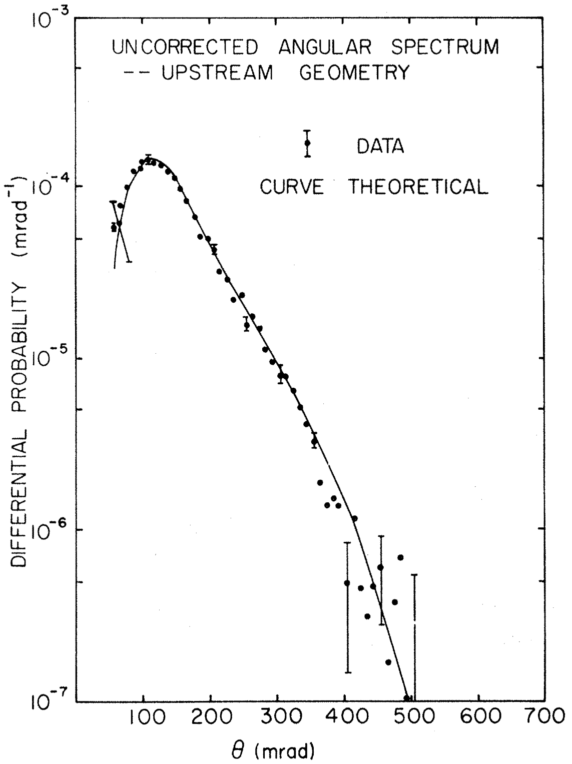

FIG. 10. Observed angular distribution for μC scattering. No correction for geometrical efficiency or multiple Coulomb scattering have been made: upstream target.

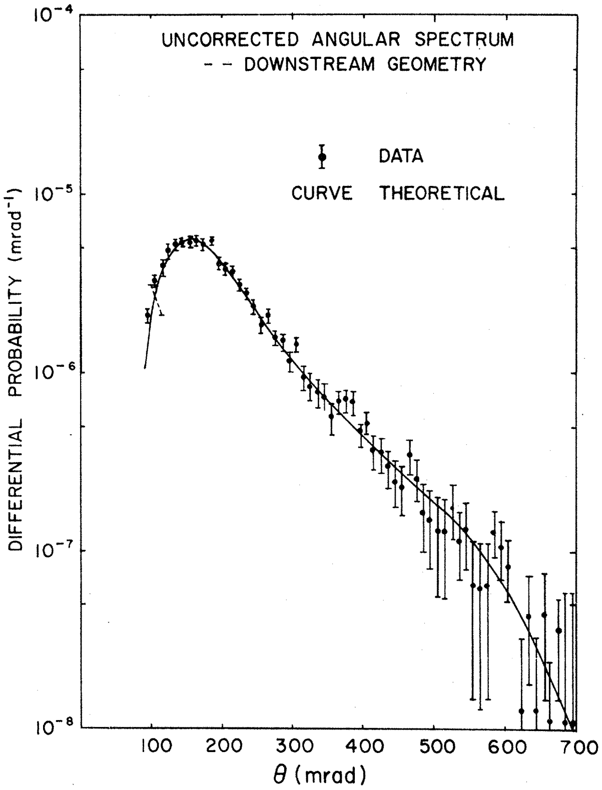

FIG. 11. Same as Fig. 10 for downstream target.

E. Inelastic Scattering

The muon scatters inelastically as well as elastically from the nucleus. Because the final momentum of the muon was not measured precisely, these inelastic events could not be rejected. The inelastic contribution to the measured scattering was estimated and subtracted using the Drell-Schwartz sum rule.[21] The total inelastic subtraction was about 5% of the data and amounted to about a 6% correction to the fitted radius. Uncertainties due to the momentum cutoff of the apparatus were negligible compared to a possible 50% uncertainty in the inelastic contribution itself.[22]

Thick-target bremmstrahlung and radiative corrections[23-25] were less than a few tenths of a percent and were neglected.

V. RESULTS

The muon-carbon differential cross section as a function of the muon scattering angle was obtained by applying the corrections previously discussed to the summed reconstructed events. The following will report: (A) the functional form that the resulting experimental cross section was fitted to in order that the rms carbon radius by extracted; (B) the results of the fit for the data combined in various ways in order that the consistency of the data, the criteria of selection, and the corrections be tested; and (C) how well the fitted results in which the rms carbon radius has been determined.

A. Form of Fitting Function

The elastic differential cross section is given by[26]

$$\frac{d\sigma}{d\Omega}=\frac{P'}{P}\,\frac{2z\alpha^2}{q^4}\,\frac{\epsilon\epsilon'+PP'\cos\theta+M_\mu{}^2}{(E'/M_c)+(\epsilon'/M_c)[1-(P/P')\cos\theta]}F(q^2)^2\equiv\left(\frac{d\sigma}{d\Omega}\right)_{\text{Mott}}F(q^2)^2\,,$$

where P, ϵ and P', ϵ' are, respectively, the initial momentum and energy, and final momentum and energy of the muon in the laboratory system. E' is the final energy of the recoil nucleus and $F(q^2)$ is the nuclear form factor. Assuming a Gaussian proton charge distribution with an rms radius R_p, the elastic shell-model form factor[27, 28] is given by

$$F(q^2)=\left(1-\frac{2-z}{6z}a_{\text{c.m.}}{}^2q^2\right)\exp\left[-\tfrac{1}{4}q^2a_{\text{c.m.}}{}^2\left(1-\frac{1}{A}\right)-\tfrac{1}{6}q^2R_p{}^2\right]$$

and the carbon radius by

$$R=\left\{\frac{2-z}{z}\,a_{\text{c.m.}}{}^2+\tfrac{3}{2}\left[a_{\text{c.m.}}{}^2\left(1-\frac{1}{A}\right)+\tfrac{2}{3}R_p{}^2\right]\right\}^{1/2}.$$

The carbon radius can thus be extracted by fitting the shell-model form factor to the experimental form factor $(d\sigma_{\text{exp}}/d\sigma_{\text{Mott}})^{1/2}$ by varying the well-length parameter $a_{\text{c.m.}}$. The rms radius found in this way is almost independent of the model. Bentz[11] put a limit of less than 0.3% on the variation of the rms radius for various charge models that are compatible with high-energy electron scattering experiments.

For scattering angles less than 500 mrad, however, the first-order Born term can be expected to be valid to only 3 to 4%.[29] Rawitscher[30, 31] has written a phase-shift program that calculates elastic lepton nuclear scattering cross sections by the exact method of partial-wave expansion. The results of his program indicate that the difference between the Born approximation and the phase-shift calculation is less than 1.5% and that over the angular region 100 to 350 mrad, the main difference is just a 1.4% increase in the phase-shift cross section compared to the Born approximation.[32] Moderate variations in the charge distribution give the same ratio $R(\theta)$, the phase-shift cross section divided by the first-order Born cross section. So rather than fit the experimental cross section using the time consuming phase-shift program and varying the charge distribution, the data were equivalently fitted by first dividing the experimental form factor by $R(\theta)$ and then by fitting the result using the Born shell-model form factor. When N, the over-all normalization of the experimental cross section, and $a_{\text{c.m.}}$ were fitted simultaneously to the experimental form factor, the effect of $R(\theta)$ was to increase N by only 0.7% and $a_{\text{c.m.}}$ by 0.01 fm.

TABLE III. Major systematic errors in the well-length parameter and the normalization.

Source of error	Percentage error in $a_{\text{c.m.}}$ (%)	Percentage error in N (%)
θ	0.3	1.2
P	0.2	0.4
Geometrical efficiency	0.5	0.2
Vertex area extrapolation	0.3	
Random-beam statistics		0.5
Total	0.7	1.4

The experimental cross-section distribution was divided into 10-mrad angular bins, and NF^2 was fitted to $(d\sigma_{\text{exp}}/d\sigma_{\text{Mott}})/R$ by simultaneously varying $a_{\text{c.m.}}$ and N, assuming $R_p=0.8$ fm. N, the uncertainty in normalization was introduced into the fit by assigning the experimental form factor the value $1.0\pm\Delta N/2$, for the $\theta=0$ angular bin.

B. Results of Fits

Figures 10 and 11 show the raw-background-subtracted angular spectrum and the results of the other corrections applied in the reverse order to the theoretical cross section. The agreement between the two was reasonable except for the small-angle regions where the corrections become quite large. In order that the effect of the uncertainties in the knowledge of geometrical efficiency, resolution, and background subtraction

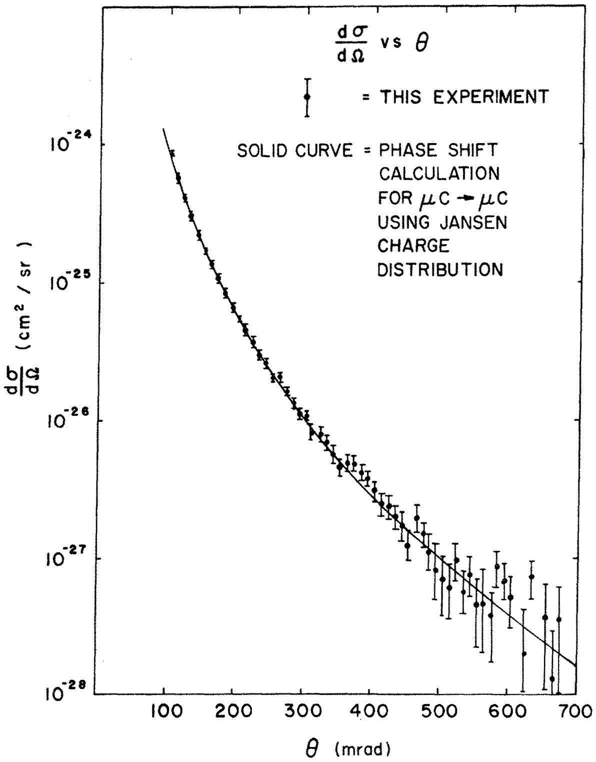

FIG. 12. Differential cross section with upstream and downstream data combined. Solid curve is the result of a phase-shift calculation using the charge distribution which provided the best fit to the electron data of Jansen, Peerdeman, and de Vries (Ref. 13).

TABLE IV. Summary of the results of previous experiments.

Authors	Technique	Method of fit	q^2 range(fm^{-2})	Fitted radius(fm)
Before 1966 (Refs. 3–8)	Elastic $eC \to eC$ and Elastic $\mu C \to eC$	Born approx.	~0.1 to 6	2.40 to 2.51
Crannel, 1966 (Ref. 9)	Elastic $eC \to eC$	Born approx.	2.8 to 11.5	2.41 low q^2 data 2.47 high q^2 data
Engfer and Turch, 1967 (Ref. 10) and Bentz, 1969 (Ref. 11)	Elastic $eC \to eC$	Phase shift	0.05 to 0.24	2.395 ± 0.028
Sick *et al.*, 1970 (Ref. 12)	Elastic $eC \to eC$	Phase shift	1 to 16	2.46 ± 0.025
Jansen *et al.*, 1970 (Ref. 13)	Elastic $eC \to eC$	Phase shift	0.02 to 0.5	2.453 ± 0.008
Backenstoss *et al.*, 1967 (Ref. 33)	Muonic x ray			2.40 ± 0.56
Shuler, 1968 (Ref. 34)	Muonic x ray			2.60 ± 0.26
This experiment	Muon elastic scattering	Born and phase-shift correction	0.016 to 0.33	$2.32^{+0.13}_{-0.18}$

could be minimized, the upstream data that covered the angular region 130 to 310 mrad were combined with the downstream data that covered the angular region 180 to 590 mrad. The fit was constrained to the angular range 130 to 590 mrad or equivalently to the q^2 region 0.0165 to 0.334 fm^{-2}.

The data of runs with differing pion contamination were fitted as a function of three β cuts. Each cut in succession removed roughly 90% of the remaining pions. The fits confirmed that pion contamination was not a problem and that the various runs were consistent within statistics. Further, all 0.6-cm carbon target events, all 0.3-cm carbon target events, all upstream events, and all downstream events were fitted. All the fitted $a_{\text{c.m.}}$ agreed with each other to within 1 standard deviation. The results of all runs combined gave

$$a_{\text{c.m.}} = 1.535^{+0.086}_{-0.12}, \quad N = 0.9986^{+0.007}_{-0.012}, \quad \chi^2 = 29,$$

for 42 degrees of freedom, where the errors are statistical only. Table III summarizes the major systematic errors in $a_{\text{c.m.}}$ and N—the uncertainty in the inelastic subtraction is ignored. The resulting rms radius is

$$R = 2.32^{+0.13}_{-0.18}\ \text{fm},$$

where the error refers to the statistical and systematic error in $a_{\text{c.m.}}$ taken in quadrature.

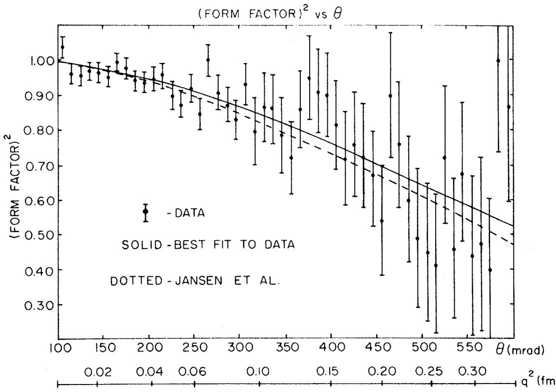

FIG. 13. Square of carbon form factor compared with prediction from electron data.

C. Comparison with Other Experiments

The rms carbon radii obtained by previous electron and muon scattering and the muonic x-ray experiments are summarized in Table IV.

The result reported here is in excellent agreement with the previous measurements. Plotted in Figs. 12 and 13 are the measured cross section and form factor and the cross section and form factor obtained using Jansen's[13] charge distribution evaluated by Rawitscher's phase-shift program for incident muons. The difference between

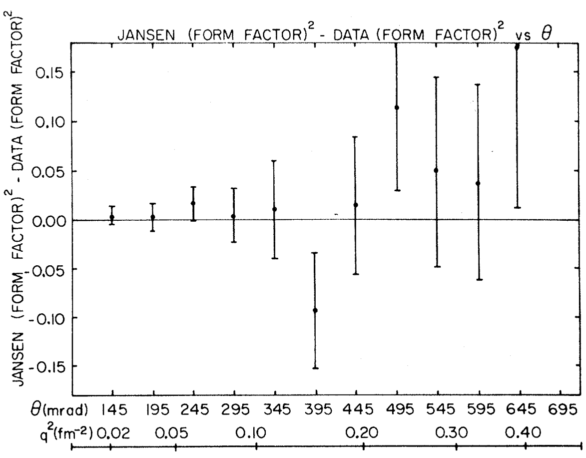

FIG. 14. Difference of squares of form factor measured with electrons and with muons as a function of angle and momentum transfer.

the Jansen form factor and the one derived here is plotted in Fig. 14.

VI. CONCLUSION

The rms radius of carbon has been redetermined by muons suffering much smaller momentum transfers than in most previous observations. In spite of this new domain of measurements, no anomalous radius terms are required, and, in fact, excellent agreement is obtained with electron-carbon data. This comparison therefore, shows no evidence for either a carbon or proton halo. Previous comparisons between muon-proton and electron-proton cross sections at high momentum transfers ($q^2 > 10$ fm^{-2}) have been shown the muon-proton cross sections to be slightly smaller (~8%) than the electron-proton cross sections.[35] The discrepancy is due quite likely to systematic experimental uncertainties; however, the difference could arise from a muon-halo[35] or from a special muon-hadron coupling.[36] The comparison made here shows no normalization difference at the level of 1.4%. Models which try to adjust the "normalization" problem by means of a halo are sensitive to moderate momentum transfers and are now bound by the data presented here.

---

*Research supported in part by the National Science Foundation.

†Present address: Rutherford Laboratory, Chilton, Didcot, Berkshire, England.

[1] R. C. Barrett, S. T. Brodsky, G. W. Erickson, and M. H. Goldhaber, Phys. Rev. 166 (1968).

[2] S. J. Brodsky, in *Fourth International Symposium on Electron and Photon Interactions at High Energies, Liverpool, 1967,* edited by D. W. Braben and R. E. Rand (Daresbury Nuclear Physics Laboratory, Daresbury, Lancashire, England, 1970), p. 17.

[3] H. Collard and R. Hofstadter, in *Nuclear Radii,* edited by H. Landolt and F. Bernstein (Springer-Verlag, Heidelberg, Germany, 1967), New Series, Group I, Vol. 2.

[4] J. H. Fregeau and R. Hofstadter, Phys. Rev. 99, 1503 (1955).

[5] J. H. Fregeau, Phys. Rev. 104, 225 (1956).

[6] H. F. Ehrenberg, R. Hofstadter, U. Meyer-Berkhout, D. G. Ravenhall, and S. E. Sobottka, Phys. Rev. 113, 666 (1959).

[7] G. E. Masek, L. D. Heggie, Y. B. Kim, and R. W. Williams, Phys. Rev. 122, 937 (1961).

[8] A. Citron, C. Delorme, D. Fries, L. Goldzahl, J. Heintze, E. G. Michaelis, C. Richard, and H. Overas, Phys. Lett. 5, 175 (1962).

[9] H. Crannell, Phys. Rev. 148, 1107 (1966).

[10] R. Engfer and D. Turck, Z. Phys. 205, 90 (1967).

[11] H. A. Bentz, Z. Naturforsch. 24A, 858 (1969).

[12] I. Sick and J. S. McCarthy, Nucl. Phys. A150, 631 (1970).

[13] J. A. Jansen, R. Th. Peerdeman, and C. de Vries, Nucl. Phys. A188, 337 (1972).

[14] L. R. B. Elton, *Nuclear Sizes* (Oxford U. P., Oxford, England, 1961), p. 41.

[15] M. Sternheim and E. Auerbach, Phys. Rev. Lett. 25, 1500 (1970).

[16] V. W. Hughes kindly loaned spark chambers 8 and 9. These chambers were constructed with 7.62×10^{-2}-mm-diam Cu wire with 7.62×10^{-1}-mm wire spacing.

[17] F. Brandamante, S. Conetti, G. Fidecato, M. Fidecato, M. Giorgi, A. Penzo, L. Piemontese, F. Salili, P. Schiavon, and A. Vascotto, in *Proceedings of the International Symposium on Nuclear Electronics, Versailles, France, 10–13 September 1968* (Société Française des Electroniciens et des Radioelectriciens, Versailles, France, 1968), Vol. III, Paper 24.

[18] G. T. Danby, S. T. Lin, and J. W. Jackson, Three Dimensional Properties of Magnetic Beam Transport Elements, Brookhaven National Laboratory internal report (unpublished).

[19] S. Goudsmit and J. L. Saunderson, Phys. Rev. 57, 24 (1940). Parameters used were those of W. T. Scott, Rev. Mod. Phys. 35, 231 (1963).

[20] E. Fermi, as quoted by B. Rossi, *High Energy Particles* (Prentice Hall, Englewood Cliffs, N. J., 1956), p. 71.

[21] S. D. Drell and C. L. Schwartz, Phys. Rev. 112, 568 (1958).

[22] M. Chen, private communication.

[23] L. W. Mo and Y. S. Tsai, Rev. Mod. Phys. 41, 205 (1969).

[24] J. W. Motz, H. Olsen, and H. W. Koch, Rev. Mod. Phys. 36, 881 (1964).

[25] L. C. Maximon, Rev. Mod. Phys. 41, 193 (1969).

[26] S. D. Drell and J. D. Walecka, Ann. Phys. (N.Y.) 28, 19 (1964).

[27] E. Amaldi, G. Fidecaro, and F. Mariani, Nuovo Cimento 7, 553 (1950).

[28] L. J. Tassie and F. C. Barker, Phys. Rev. 111, 940 (1958).

[29] J. M. Jauch and F. Rohrlich, *Theory of Photons and Electrons* (Addison-Wesley, Reading, Mass., 1955), p. 331.

[30] G. H. Rawitscher, Phys. Rev. 112, 1274 (1958).

[31] G. H. Rawitscher and C. R. Fischer, Phys. Rev. 122, 1330 (1961).

[32] L. Cardman of Yale University kindly supplied us a copy of G. H. Rawitscher's program.

[33] G. Backenstoss, S. Charalambus, H. Daniel, H. Kock, G. Poelz, H. Schmitt, and L. Tauscher, Phys. Lett. 25B, 547 (1967).

[34] W. B. Shuler, Ph. D. thesis, College of William and Mary, 1968 (unpublished).

[35] T. J. Braunstein, W. L. Lawn, F. Martin, M. L. Perl, W. T. Tenet, and T. F. Zipf, SLAC-PUB-1009, 1972 (unpublished), (TH) and (EXP).

[36] S. Barshay, Phys. Lett. 37B, 397 (1971).